CHALMERS
UNIVERSITY OF TECHNOLOGY

Effects of lithium insertion induced swelling of a structural battery negative electrode

Downloaded from: https://research.chalmers.se, 2024-10-12 04:07 UTC

Citation for the original published paper (version of record):
Larsson, C., Larsson, F., Xu, J. et al (2023). Effects of lithium insertion induced swelling of a structural battery negative electrode. Composites Science and Technology, 244.
http://dx.doi.org/10.1016/j.compscitech.2023.110299

N.B. When citing this work, cite the original published paper.

research.chalmers.se offers the possibility of retrieving research publications produced at Chalmers University of Technology. It covers all kind of research output: articles, dissertations, conference papers, reports etc. since 2004. research.chalmers.se is administrated and maintained by Chalmers Library

(article starts on next page)

Composites Science and Technology 244 (2023) 110299

Contents lists available at ScienceDirect

Composites Science and Technology

journal homepage: www.elsevier.com/locate/compscitech

Effects of lithium insertion induced swelling of a structural battery negative electrode

Carl Larsson *, Fredrik Larsson, Johanna Xu, Kenneth Runesson, Leif E. Asp

Department of Industrial and Materials Science, Chalmers University of Technology, Gothenburg, SE-412 96, Sweden

ARTICLE INFO

Keywords:
C. Computational mechanics
C. Representative volume element (RVE)
C. Multiscale modelling
C. Material modelling
A. Multifunctional composites

ABSTRACT

Structural battery composites fall under the category multifunctional materials with the ability to simultaneously store electrical energy and carry mechanical load. While functioning as the negative electrode, the carbon fibres also act as mechanical reinforcement. Lithium ion insertion in the carbon fibres is accompanied by a large radial expansion of 6.6 % and an axial expansion of 0.85 % of the fibres. Furthermore, the elastic moduli of the carbon fibres are significantly affected by the insertion of lithium. Current structural battery modelling approaches do not consider these features. In this paper, we investigate the effect of lithium insertion in carbon fibres on the structural electrode mechanical properties by developing a computational model considering finite strains and lithium concentration dependent fibre moduli. The computational model enables representation of morphological change, whereby, features such as internal stress state, homogenized tangent stiffness and effective expansion of the electrode caused by carbon fibre lithiation can be predicted. The adopted finite strain formulation allows for consistent consideration of measurement data at varying state of lithiation. The significance of adopting the finite strain formulation is also shown numerically. Finally, by implementing a novel approach to homogenized stress-free expansion, it is shown that the computed expansion of the structural electrode follows a similar trend to what is observed from experiments.

1. Introduction

In structural battery composites, carbon fibres are used as negative electrode material with a multifunctional purpose; to store energy as a lithium host, to conduct electrons as current collector, and to carry mechanical loads as reinforcement [1–4]. Carbon fibres are also used in the positive electrode, where they serve as reinforcement and current collector, as well as a substrate for the cathode material coating [5, 6]. The carbon fibres are embedded in a bicontinuous porous matrix material, herein referred to as structural battery electrolyte (SBE), consisting of a solid polymer phase transferring mechanical loads, and pores containing liquid electrolyte facilitating ion transport [7]. Kjell et al. studied the electrochemical performance of T800 carbon fibres in liquid electrolyte [8]. They found the reversible capacity of desized T800 carbon fibres to be approximately 58 % of the first cycle capacity at lithiation with a first cycle loss of 35 %. Furthermore, they found a strong rate effect on capacity for the T800 fibre, ranging from approximately 140 mAh/g at 1C to almost 300 mAh/g at C/10. These results were later confirmed by Carlstedt et al. [9]. Duan et al. explored effects of lithium insertion, i.e. lithiation, of single IMS65 carbon fibres on fibre moduli and dimension [10]. It was reported that the fibres longitudinal modulus E_L^f is reduced by 12 %, accompanied by an axial expansion of 0.69 % upon lithiation. In addition, the transverse fibre modulus E_T^f increased by 107 %, and the fibre diameter increased by 6.6 % as the IMS65 carbon fibre was fully lithiated. In an accompanying study, Carlstedt et al. investigated lithiation induced swelling of T800 carbon fibre tows in liquid electrolyte as well as embedded in a SBE matrix [9]. The relative (stress free) expansion of carbon fibres in liquid electrolyte was approximately 0.85 %, whereas the carbon fibre tow embedded in SBE expanded 0.72 %. The extensive volume change of the fibre during electrochemical cycling gives raise to substantial changes in the composite's internal stress state. The coupled electro-chemo-mechanical processes in a structural negative electrode, and the effects on internal stresses, have been addressed by Carlstedt and co-workers [9,11,12].

In a related study, Grazioli et al. analysed how transport of lithium ions through solid polymer electrolyte (SPE), affects the local stress and strain distributions across the SPE using a multiphysics numerical model [13]. Local strains up to 12 % in the SPE were predicted as lithium ions migrate between the electrodes. Similar studies have been performed by Bucci et al. who developed a computational model in finite strain setting, studying concentration distributions and the accompanying swelling of different species, as well as their effect on the

* Corresponding author.
E-mail address: calar@chalmers.se (C. Larsson).

https://doi.org/10.1016/j.compscitech.2023.110299
Received 22 June 2023; Received in revised form 2 October 2023; Accepted 5 October 2023
Available online 10 October 2023
0266-3538/© 2023 The Authors. Published by Elsevier Ltd. This is an open access article under the CC BY license (http://creativecommons.org/licenses/by/4.0/).

internal stress state [14]. Moreover, coupled electro-chemo-mechanical models in finite strain setting for binary solid electrolytes were studied by Ganser et al. [15]. They showed a significant contribution to both electrochemical and mechanical response by accounting for the change of transport path due to swelling effects.

State-of-the-art coupled electro-chemo-mechanical models for structural battery composites developed by Carlstedt et al. considers small strain setting [11]. However, volume changes due to lithium insertion are large and particularly important to consider for load carrying materials. In this paper, we formulate a computational model in finite strain setting, addressing the swelling/shrinkage of T800 carbon fibres due to lithium insertion/desertion. The computational model allows for predictions of local stresses accounting for large deformations and computation of effective swelling of the homogenized structural battery electrode. Predicted electrode swelling is compared to experimental data. Moreover, changes in the computed homogenized mechanical properties of the electrode caused by carbon fibre lithiation is assessed. The importance of the finite strain formulation is evaluated by comparison to predictions using a linear, small strain model for local stress and stiffness results.

2. Modelling of the structural battery composite

2.1. Preliminaries

The microscale analysis is performed on a synthetical, assumed representative volume element (RVE). The RVE domain, $\Omega_{X,\square}$ indicated by the box $\square$, consists of the carbon fibre domain, $\Omega^{\mathrm{cf}}_{X,\square}$, and the SBE domain, $\Omega^{\mathrm{SBE}}_{X,\square}$, with $\Omega_{X,\square} = \Omega^{\mathrm{cf}}_{X,\square} \cup \Omega^{\mathrm{SBE}}_{X,\square}$ as illustrated in Fig. 1. We stress that the framework presented in this paper is applicable to arbitrary size and architecture RVE. However, this study is restricted to a single RVE realization for illustration of the method. The typical cross sectional area of the electrode (macroscale domain) is 50 x 15 000 μm^2 (thickness × width) [9,16]. From a computational point of view, it is intractable to resolve the electrode on the microscale using DNS (direct numerical simulations). Further, separation of scales holds at the structural scale.

In order to analyse effects of lithiation/delithiation of the carbon fibres on the performance of a structural battery, knowledge about the charge cycle and rate is needed. The state of lithiation is defined as

$$c(t) = \frac{c_{Li}(t)}{c^{\max}_{Li}} \tag{1}$$

where $c_{Li}(t)$ is the concentration of lithium, and $c^{\max}_{Li}$ denotes the reference maximum concentration of lithium, for a certain charge rate. Eq. (1) is applicable for conditioned fibres, i.e., when studying fibres with a reversible capacity in the structural electrode. However, for unconditioned fibres the varying maximum lithium concentration with respect to charge cycle must be considered. The state of lithiation for charge cycle i, $(c(t))_i$, is expressed as

$$(c(t))_i = \frac{c_{Li}(t)}{(c^{\max}_{Li})_i}, \tag{2}$$

where $(c^{\max}_{Li})_i$ represents the reference maximum concentration that can be inserted into the electrode during the ith lithium insertion/desertion cycle. At any time t, for given spatial distribution of c inside the fibres, the mechanical response can be determined instantaneously, as described subsequently. In this paper, we do not model Li-ion transport, nor do we utilize measurement data for spatial distribution of c inside the fibres. Therefore, in view of the experimental verification examples in Section 3.4, we restrict to the extreme situation of considering c being uniform inside $\Omega^{\mathrm{cf}}_{X,\square}$. During electrochemical cycling, the carbon fibres expand and contract due to lithium insertion and desertion. These volume changes cause internal stresses in the composite. The internal stresses that arise due to lithiation are affected by the external boundary conditions acting on the composite. If the composite is not allowed to expand, i.e., is externally constrained as illustrated in Fig. 1b, high magnitude of the internal stresses are expected. In contrast, lower magnitudes are expected if the composite is unconstrained, allowing for free expansion as illustrated in Fig. 1c.

2.2. The RVE problem

In this section we formulate the periodic RVE-problem in the finite strain setting in terms of solving the linear momentum balance and imposing periodic boundary conditions similar to [17–20]. The boundary value problem is stated as

$$-\boldsymbol{P}\cdot\boldsymbol{\nabla}_X = \boldsymbol{0} \text{ in } \Omega_{X,\square}, \tag{3a}$$

$$[\![\boldsymbol{u}]\!]_\square = [\bar{\boldsymbol{F}} - \boldsymbol{I}]\cdot[\boldsymbol{X}^+ - \boldsymbol{X}^-] \text{ on } \Gamma^+_{X,\square}, \tag{3b}$$

$$(\boldsymbol{P}\cdot\boldsymbol{N})^+ + (\boldsymbol{P}\cdot\boldsymbol{N})^- = \boldsymbol{0} \text{ on } \Gamma^+_{X,\square}, \tag{3c}$$

with the boundary decomposed as $\partial\Omega_{X,\square} = \Gamma^+_{X,\square} \cup \Gamma^-_{X,\square}$, where $\Gamma^+_{X,\square}$ and $\Gamma^-_{X,\square}$ are the image and mirror boundaries, respectively. $\varphi^{\mathrm{PER}} : \Gamma^+_{X,\square} \to \Gamma^-_{X,\square}$ defines periodicity mapping of mirrored points $\boldsymbol{X}^-(\boldsymbol{X})$ for $\boldsymbol{X} \in \Gamma^+_{X,\square}$. Consequently, we may express $f^-(\boldsymbol{X}) = f(\varphi^{\mathrm{PER}}(\boldsymbol{X}))$ and $f^+(\boldsymbol{X}) = f(\boldsymbol{X})$ for any function $f(\boldsymbol{X})$. Furthermore, the jump operator is defined as $[\![\bullet]\!]_\square := \bullet^+ - \bullet^-$, $\boldsymbol{P}$ represents the first Piola–Kirchhoff stress tensor, $\boldsymbol{\nabla}_X$ is the gradient operator in the delithiated (reference) configuration $\Omega_{X,\square}$, and $\boldsymbol{N}$ is the outwards facing unit normal. $\boldsymbol{F}$ is the deformation gradient, $\boldsymbol{I}$ the second order identity and $\boldsymbol{X}$ represents the reference coordinate. The problem is completed by introducing stress–strain relations in the fibre ($\Omega^{\mathrm{cf}}_{X,\square}$) and SBE ($\Omega^{\mathrm{SBE}}_{X,\square}$), respectively. These models are detailed in Section 2.3, where the key modelling assumption is that $\boldsymbol{P} = \boldsymbol{P}(c, \boldsymbol{F})$ in the fibre domain, while $\boldsymbol{P} = \boldsymbol{P}(\boldsymbol{F})$ in the SBE. The displacement field is decomposed as $\boldsymbol{u} = \boldsymbol{u}^{\mathrm{M}} + \boldsymbol{u}^{\mathrm{s}}$, with the macroscopic part $\boldsymbol{u}^{\mathrm{M}} = [\bar{\boldsymbol{F}} - \boldsymbol{I}]\cdot[\boldsymbol{X} - \bar{\boldsymbol{X}}]$ and the microscopic (subscale) part $\boldsymbol{u}^{\mathrm{s}}$. Hence, from Eq. (3b) we emphasize that it is the microscopic part which is periodic. Here, $\bar{\boldsymbol{F}}$ denotes the homogenized (macroscopic) deformation gradient of the composite. The local deformation gradient is thus expressed as $\boldsymbol{F} = \boldsymbol{I} + [\boldsymbol{u}\otimes\boldsymbol{\nabla}_X] = \bar{\boldsymbol{F}} + \boldsymbol{u}^{\mathrm{s}}\otimes\boldsymbol{\nabla}_X$. The decomposition of $\boldsymbol{u}$ with periodicity is illustrated in Fig. 2. Finally, the deformation controlled problem for given concentration c is stated in the weak format: Find $\boldsymbol{u}^{\mathrm{s}}\{c, \bar{\boldsymbol{F}}\} = \boldsymbol{u}^{\mathrm{s}} \in \mathbb{U}_\square$, such that

$$\frac{1}{|\Omega_{X,\square}|}\int_{\Omega_{X,\square}} \boldsymbol{P}(c, \bar{\boldsymbol{F}} + \boldsymbol{u}^{\mathrm{s}}\otimes\boldsymbol{\nabla}_X) : [\delta\boldsymbol{u}^{\mathrm{s}}\otimes\boldsymbol{\nabla}_X]\mathrm{d}\Omega_X = 0 \quad \forall\delta\boldsymbol{u}^{\mathrm{s}} \in \mathbb{U}_\square, \tag{4}$$

where $\mathbb{U}_\square = \left\{ \boldsymbol{v} \in [\mathbb{H}^1(\Omega_{X,\square})]^3 \ : \ [\![\boldsymbol{v}]\!] = 0 \text{ on } \Gamma^+_{X,\square} \right\}$ and $\mathbb{H}^1(\Omega_{X,\square})$ is the space of functions with square integrable derivatives of order zero and one on the domain $\Omega_{X,\square}$. The effective (macroscopic) first Piola–Kirchhoff stress denoted $\bar{\boldsymbol{P}}$, is computed as the volume average[1]

$$\bar{\boldsymbol{P}}\{c, \bar{\boldsymbol{F}}\} := \frac{1}{|\Omega_{X,\square}|}\int_{\Omega_{X,\square}} \boldsymbol{P}(c, \bar{\boldsymbol{F}} + \boldsymbol{u}^{\mathrm{s}}\{c, \bar{\boldsymbol{F}}\}\otimes\boldsymbol{\nabla}_X)\mathrm{d}\Omega_X, \tag{5}$$

and the homogenized tangent stiffness is expressed as

$$\bar{\mathsf{L}}\{c, \bar{\boldsymbol{F}}\} = \frac{\mathrm{d}\bar{\boldsymbol{P}}}{\mathrm{d}\bar{\boldsymbol{F}}}. \tag{6}$$

For the case when composite expansion is restricted, we control the macroscopic deformation gradient $\bar{\boldsymbol{F}}$ such that $\bar{\boldsymbol{F}} = \boldsymbol{I}$ and compute the *constrained*, homogenized stress and tangent stiffness are defined as

$$\bar{\boldsymbol{P}}_{\mathrm{CON}}\{c\} = \bar{\boldsymbol{P}}\{c, \boldsymbol{I}\}, \tag{7a}$$

$$\bar{\mathsf{L}}_{\mathrm{CON}}\{c\} = \bar{\mathsf{L}}\{c, \boldsymbol{I}\}. \tag{7b}$$

To represent an *unconstrained* composite, i.e. stress free expansion, we control the homogenized stress and seek a macroscopic deformation. To

[1] $\{\bullet\}$ denotes implicit dependence on the argument.

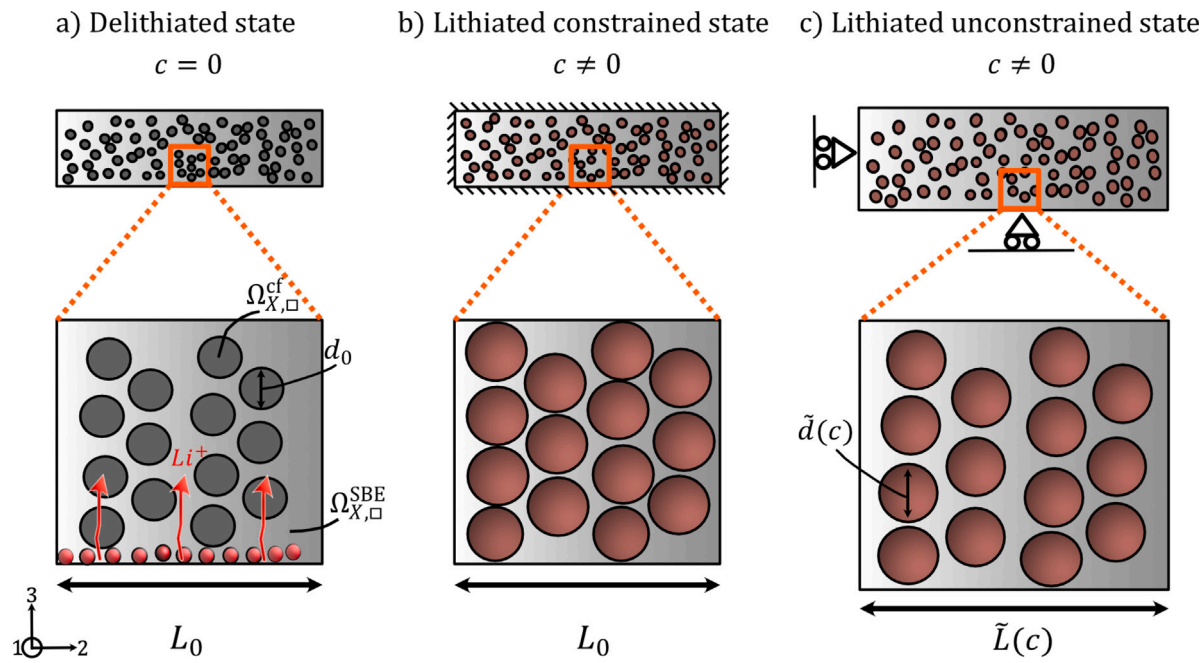

Fig. 1. Two-dimensional illustration of morphology change as carbon fibres are lithiated. (a) Delithiated RVE with initial side length L_0 and carbon fibre diameter d_0. (b) Lithiated, fully constrained, RVE such that the side length remains at L_0. (c) Lithiated, unconstrained RVE, whereby the side length increases, $\tilde{L}(c) > L_0$.

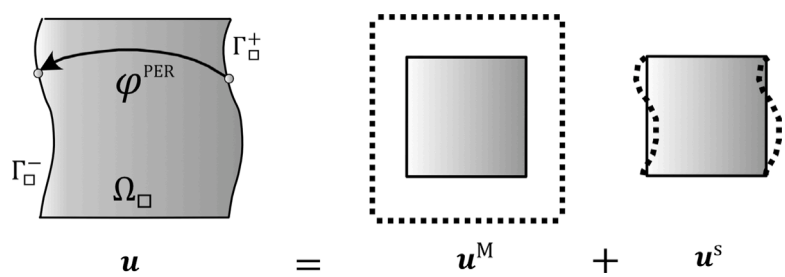

Fig. 2. Two-dimensional illustration of the homogeneous RVE domain, $\Omega_\square$, in deformed configuration with appurtenant boundaries, $\partial\Omega_\square$. The displacement field, $\boldsymbol{u}$, is decomposed into a macroscopic part, $\boldsymbol{u}^M$, and a microscopic fluctuation, $\boldsymbol{u}^s$.

ensure uniqueness of the solution, the model is formulated in terms of the right stretch tensor $\bar{\boldsymbol{U}}$ and the Biot stress $\bar{\boldsymbol{T}} = [\bar{\boldsymbol{R}} \cdot \bar{\boldsymbol{P}}]^{sym}$, where $\bar{\boldsymbol{R}}$ is the macroscopic rotation. The detailed formulation is outlined in Appendix A. Thereby, in mixed format, we seek $\boldsymbol{u}^s\{c, \bar{\boldsymbol{T}}\} = \boldsymbol{u}^s \in \mathbb{U}_\square$ and $\bar{\boldsymbol{U}}\{c, \bar{\boldsymbol{T}}\} = \bar{\boldsymbol{U}} \in \mathbb{R}^{3\times3}_{sym}$ such that

$$\frac{1}{|\Omega_{X,\square}|}\int_{\Omega_{X,\square}} \boldsymbol{P}(c, \bar{\boldsymbol{U}} + \boldsymbol{u}^s \otimes \boldsymbol{\nabla}_X) : [\delta\boldsymbol{u}^s \otimes \boldsymbol{\nabla}_X] \mathrm{d}\Omega_X = 0 \quad \forall \delta\boldsymbol{u}^s \in \mathbb{U}_\square, \tag{8a}$$

$$\frac{1}{|\Omega_{X,\square}|}\int_{\Omega_{X,\square}} \boldsymbol{P}(c, \bar{\boldsymbol{U}} + \boldsymbol{u}^s \otimes \boldsymbol{\nabla}_X) \mathrm{d}\Omega_X : \delta\bar{\boldsymbol{U}} = 0 \quad \forall \delta\bar{\boldsymbol{U}} \in \mathbb{R}^{3\times3}_{sym}. \tag{8b}$$

Finally, we can determine the unconstrained deformation gradient as

$$\bar{\boldsymbol{F}}_{UNCON}\{c\} = \bar{\boldsymbol{U}}\{c, \boldsymbol{0}\}, \tag{9a}$$

and, using Eq. (6), we express the unconstrained tangent stiffness as

$$\bar{\mathsf{L}}_{UNCON}\{c\} = \bar{\mathsf{L}}\{c, \bar{\boldsymbol{F}}_{UNCON}\{c\}\}. \tag{9b}$$

Remark: We note that Eq. (9a) pertains to the assumed rotation $\bar{\boldsymbol{R}} = \boldsymbol{I}$. Due to rigid-body invariance, any rotation $\bar{\boldsymbol{R}}$ results in $\boldsymbol{u}^s = \bar{\boldsymbol{R}} \cdot \boldsymbol{u}^s\{c, \boldsymbol{0}\}$, $\bar{\boldsymbol{F}} = \bar{\boldsymbol{R}} \cdot \bar{\boldsymbol{U}}_{UNCON}$, $\bar{\boldsymbol{P}} = \bar{\boldsymbol{R}} \cdot \boldsymbol{0} = \boldsymbol{0}$. □

2.3. Constitutive models

2.3.1. Constitutive model for the fibre domain, $\Omega^{cf}_\square$

Consider a fibre that swells due to lithium insertion with uniform concentration c. In the finite deformation setting, we adopt a multiplicative decomposition of the deformation gradient as

$$\boldsymbol{F} = \tilde{\boldsymbol{F}} \cdot \boldsymbol{F}^{ch}(c)\,, \quad \boldsymbol{F}^{ch}(c) = \left(\boldsymbol{I} + [\alpha^{ch}_L \boldsymbol{m}_1 + \alpha^{ch}_T(\boldsymbol{m}_2 + \boldsymbol{m}_3)]c\right), \tag{10}$$

where $\boldsymbol{F}^{ch}(c)$ contributes to a chemical expansion and $\tilde{\boldsymbol{F}}$ represents an elastic deformation as illustrated in Fig. 3. Moreover, $\boldsymbol{m}_i := \boldsymbol{e}_i \otimes \boldsymbol{e}_i$ is the ith base dyad, α^{ch}_L and α^{ch}_T are the longitudinal and transverse lithium insertion expansion coefficients, respectively. $\boldsymbol{F}^{ch}(c)$ may be large, even for small elastic deformations ($\tilde{\boldsymbol{F}}$ close to $\boldsymbol{I}$). The longitudinal chemical expansion coefficient α^{ch}_L was measured by Carlstedt et al. and the transverse chemical expansion coefficient α^{ch}_T was measured by Duan et al. [9,10]. To model elasticity for stress free deformation, we express the volume specific free energy for a given state of lithiation c as

$$\psi_X(c, \boldsymbol{F}) = J^{ch}\tilde{\psi}(c, \tilde{\boldsymbol{F}}), \tag{11}$$

where $J^{ch} = \det(\boldsymbol{F}^{ch}(c))$ and $\tilde{\psi}$ is the free energy per unit volume in the lithiated configuration $\tilde{B}$. The pertinent intermediate first Piola–Kirchhoff stress tensor becomes

$$\tilde{\boldsymbol{P}} = \frac{\partial\tilde{\psi}}{\partial\tilde{\boldsymbol{F}}} = \frac{1}{J^{ch}(c)}\boldsymbol{P} \cdot [\boldsymbol{F}^{ch}(c)]^T, \tag{12}$$

where $\boldsymbol{P} = \frac{\partial\psi_X}{\partial\boldsymbol{F}}$ denotes the conventional first Piola–Kirchhoff stress tensor w.r.t. the reference configuration B_X, i.e., the equilibrium stress. Duan et al. experimentally measured the longitudinal and transverse moduli E_L and E_T, on unconstrained carbon fibres for varying state of lithiation [10]. Consequently, the moduli are measured after the

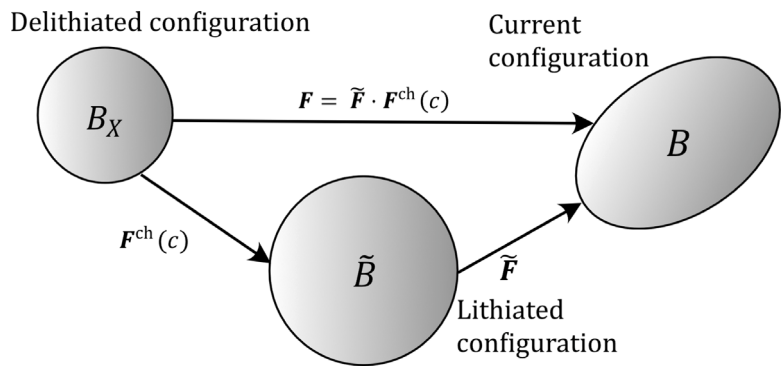

Fig. 3. Multiplicative split of the deformation gradient in the carbon fibre. Starting from the delithiated (reference) configuration B_X, the domain is expanded to $\tilde{B}$ after lithiation (function of c), finally deformed elastically to B.

chemical deformation $\boldsymbol{F}^{\mathrm{ch}}(c)$, and are included in the apparent linear elasticity "Hooke" tensor $\tilde{\mathsf{E}}(c)$, with detailed description formulated in Appendix B. In the lithiated configuration $\tilde{B}$, we express the intermediate first Piola–Kirchhoff stress using the Saint-Venant model from the lithiated configuration $\tilde{B}$ as

$$\tilde{\boldsymbol{P}} = \tilde{\boldsymbol{F}} \cdot \tilde{\boldsymbol{S}} \text{ with } \tilde{\boldsymbol{S}}(c, \tilde{\boldsymbol{E}}) = \tilde{\mathsf{E}}(c) : \tilde{\boldsymbol{E}} \tag{13a}$$

where

$$\tilde{\boldsymbol{E}} := \frac{1}{2}[\tilde{\boldsymbol{C}} - \boldsymbol{I}], \ \tilde{\boldsymbol{C}} = \tilde{\boldsymbol{F}}^T \cdot \tilde{\boldsymbol{F}} = [\boldsymbol{F}^{\mathrm{ch}}]^{-T} \cdot \boldsymbol{C} \cdot [\boldsymbol{F}^{\mathrm{ch}}]^{-1} \tag{13b}$$

Linearization of Eqs. (13) verifies that $\tilde{\mathsf{E}}(c)$ is precisely the apparent linear elasticity tangent stiffness for a stress free, lithiated, carbon fibre. $\tilde{\boldsymbol{S}}$ is the intermediate second Piola–Kirchhoff stress tensor and $\tilde{\boldsymbol{E}}$ is the corresponding Green Lagrange strain. Combining Eqs. (12) and (13) we may express the first Piola–Kirchhoff stress as

$$\boldsymbol{P}(c, \boldsymbol{F}) = J^{\mathrm{ch}}(c)\tilde{\boldsymbol{P}}(c, \boldsymbol{F}) \cdot [\boldsymbol{F}^{\mathrm{ch}}(c)]^{-T}, \tag{14}$$

where $\tilde{\boldsymbol{P}}(c, \boldsymbol{F})$ was given in Eq. (13a). This is the complete model parametrized in the concentration c. In summary, the model in Eq. (14) is calibrated from measurement of $\boldsymbol{F}^{\mathrm{ch}}(c)$, as presented in Eq. (10), and the apparent linear elastic properties $\mathsf{E}(c)$, used in the Saint-Venant model (13b). While the Saint-Venant model represents the measured elastic response for $\tilde{\boldsymbol{F}} = \boldsymbol{I}$, there is no limitation on $\boldsymbol{F}^{\mathrm{ch}}(c)$. The mechanical properties of the carbon fibres are presented in Table B.1.

2.3.2. Constitutive model for the structural battery electrolyte domain, $\Omega^{SBE}_{\square}$

We apply an isotropic hyperelastic neo-Hookean material model for the SBE matrix, whereby the second Piola–Kirchhoff stress is decomposed additively into volumetric- and isochoric parts. Thereby,

$$\boldsymbol{P}(\boldsymbol{F}) = \boldsymbol{F} \cdot \boldsymbol{S}(\boldsymbol{C}), \tag{15a}$$

$$\boldsymbol{S}(\boldsymbol{C}) = KJ[J-1]\boldsymbol{C}^{-1} + GJ^{-2/3}\left[\boldsymbol{I} - \frac{1}{3}(\boldsymbol{C} : \boldsymbol{I})\boldsymbol{C}^{-1}\right], \tag{15b}$$

where $J = \det(\boldsymbol{F}) = \sqrt{\det \boldsymbol{C}}$, K is the bulk modulus and G is the shear modulus of the SBE. Based on existing measurements of linear elastic isotropic material parameters, we choose the neo-Hookean model to be able to account for large volumetric deformations. The mechanical properties of the SBE are presented in Table B.1. This is not likely to be an accurate model for the SBE, in particular for large compression. However, pending more elaborate measurement data we consider neo-Hooke as one possible extension of linear elasticity.

3. Results and discussion

In this section, the proposed modelling framework will be utilized to predict the composite properties of a negative structural electrode. The chosen fibre architecture for the following RVE analyses is similar to the arrangement used in Carlstedt et al. referred to as a repeatable unit [9,21]. In the subsequent investigations, we will keep this fibre arrangement but vary the volume fractions. In Sections 3.1–3.3 we choose a fibre volume fraction of 43 % in accordance with SEM image observations by Asp et al. and Siraj et al. [2,16]. In Section 3.4, we compare the model results to the existing experiment by Carlstedt et al. where the fibre volume fraction was estimated to be around 20 % [9]. Thereby, the fibre volume fraction is adjusted to 20 % for this specific case. In all performed analyses, we model the geometry in 3D using linear tetrahedral elements, integrated numerically using single Gauss point quadrature.

3.1. Preliminary model assessment

In the following analysis we let the state of lithiation vary from the delithiated state ($c = 0$) to the fully lithiated state ($c = 1$). The constrained homogenized stresses and unconstrained homogenized deformation gradients are computed as defined in Eqs. (7a) and (9a), respectively. Fig. 4 shows the variation of the 22 (transverse) component of $\bar{\boldsymbol{P}}_{CON}$ and $\bar{\boldsymbol{F}}_{UNCON} - 1$ with respect to c, compared to the variation of the corresponding small strain quantity with respect to c. When c grows large, the stress magnitude deviate between finite and small strains, whereas the strain magnitude does not exhibit a significant difference.

In order to investigate the local features of the constituents, we shall evaluate averages on the fibre ($\Omega^{\mathrm{cf}}_{X,\square}$) and SBE ($\Omega^{\mathrm{SBE}}_{X,\square}$) domains. The average first Piola–Kirchhoff stresses for each domain are computed as

$$\bar{\boldsymbol{P}}^{\mathrm{cf}}\{c, \bar{\boldsymbol{F}}\} = \frac{1}{|\Omega^{\mathrm{cf}}_{X,\square}|}\int_{\Omega^{\mathrm{cf}}_{X,\square}} \boldsymbol{P}(c, \bar{\boldsymbol{F}} + \boldsymbol{u}^{\mathrm{s}}\{\bar{\boldsymbol{F}}\} \otimes \boldsymbol{\nabla}_X)\mathrm{d}\Omega_X, \tag{16a}$$

$$\bar{\boldsymbol{P}}^{\mathrm{SBE}}\{c, \bar{\boldsymbol{F}}\} = \frac{1}{|\Omega^{\mathrm{SBE}}_{X,\square}|}\int_{\Omega^{\mathrm{SBE}}_{X,\square}} \boldsymbol{P}(c, \bar{\boldsymbol{F}} + \boldsymbol{u}^{\mathrm{s}}\{\bar{\boldsymbol{F}}\} \otimes \boldsymbol{\nabla}_X)\mathrm{d}\Omega_X, \tag{16b}$$

and the domain-wise average deformation gradients are computed as

$$\bar{\boldsymbol{F}}^{\mathrm{cf}} = \frac{1}{|\Omega^{\mathrm{cf}}_{X,\square}|}\int_{\Omega^{\mathrm{cf}}_{X,\square}} [\bar{\boldsymbol{F}} + \boldsymbol{u}^{\mathrm{s}}\{\bar{\boldsymbol{F}}\} \otimes \boldsymbol{\nabla}_X]\mathrm{d}\Omega_X, \tag{17a}$$

$$\bar{\boldsymbol{F}}^{\mathrm{SBE}} = \frac{1}{|\Omega^{\mathrm{SBE}}_{X,\square}|}\int_{\Omega^{\mathrm{SBE}}_{X,\square}} [\bar{\boldsymbol{F}} + \boldsymbol{u}^{\mathrm{s}}\{\bar{\boldsymbol{F}}\} \otimes \boldsymbol{\nabla}_X]\mathrm{d}\Omega_X. \tag{17b}$$

Fig. 5 shows the homogenized stress–strain relationships for carbon fibre and SBE domains, respectively, as c increases. In Figs. 5a and 5b the RVE is constrained. Hence, expansion is prohibited, causing compressive stresses along the fibres, in the 11-direction, as shown in Fig. 5a. The stress–strain relationship in the 22-direction is shown in Fig. 5b. As the carbon fibres expand ($\bar{F}_{22}$ increases) the SBE is loaded in compression, restricting the free expansion of the carbon fibres. In Figs. 5c and 5d results for the unrestricted, freely expanding, RVE are presented. Here, both the fibres and SBE are found to expand in the 11-

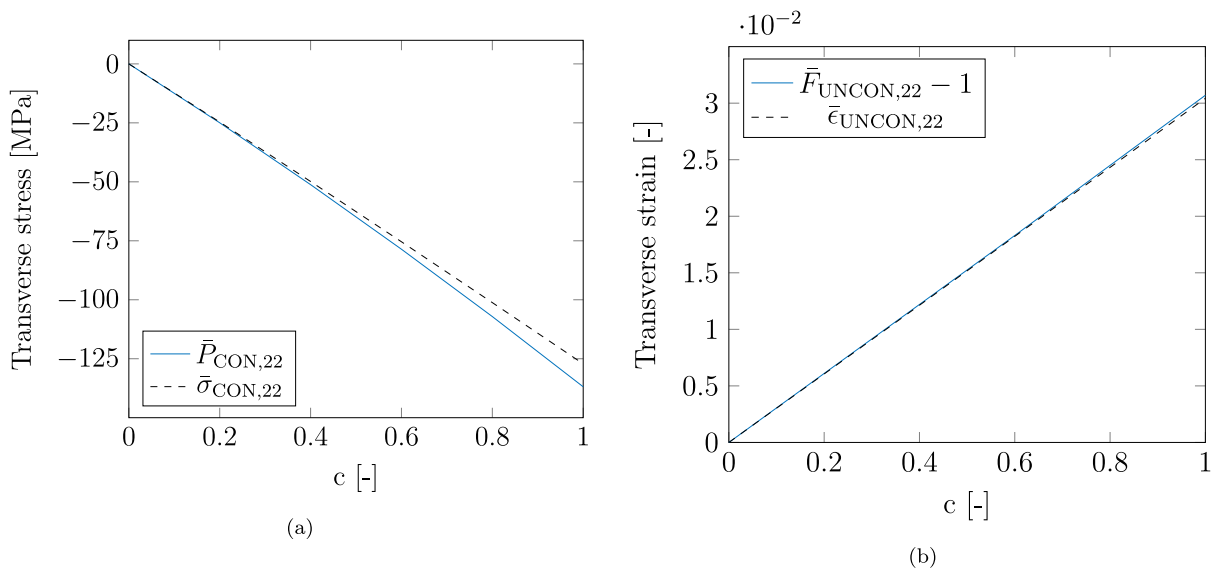

Fig. 4. (a) Constrained homogenized transverse stress versus state of lithiation (c) in the finite deformation setting ($\bar{P}_{\mathrm{CON},22}$) as well as for the small strain approximation ($\bar{\sigma}_{\mathrm{CON},22}$). (b) Unconstrained homogenized transverse strain versus state of lithiation (c) in the finite deformation setting ($\bar{F}_{\mathrm{UNCON},22} - 1$) as well as for the small strain approximation ($\bar{\epsilon}_{\mathrm{UNCON},22}$).

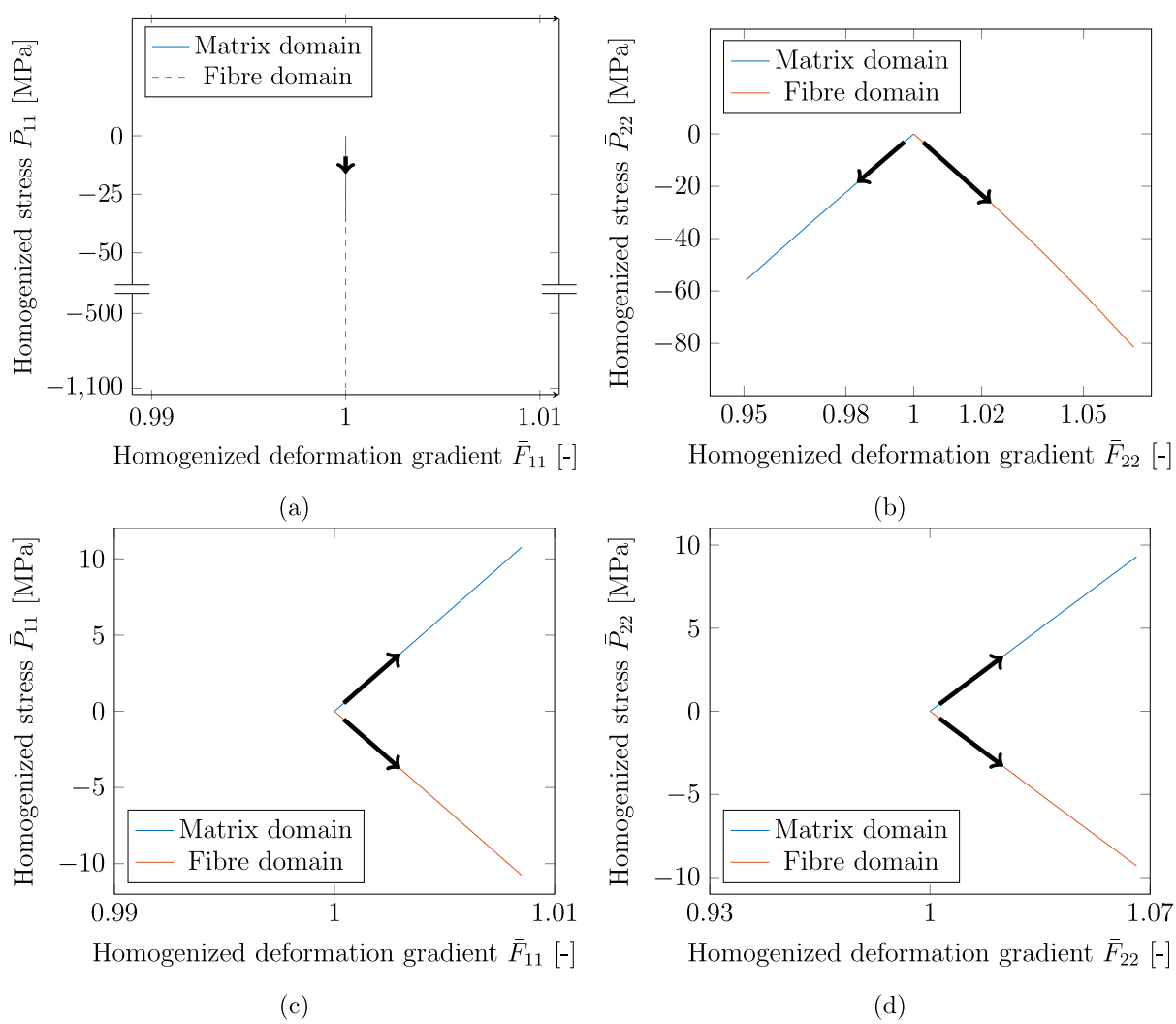

Fig. 5. Domain-wise homogenized quantities, defined in Eqs. (16) and (17) as the state of lithiation c varies linearly from $c = 0$ to $c = 1$, (indicated by arrows). The components of the homogenized quantities are consistent with the coordinate system presented in Fig. 1. (a) Domain-wise 11-component of $\bar{\boldsymbol{P}}$ versus $\bar{\boldsymbol{F}}$ for the constrained case. (b) Domain-wise 22-component of $\bar{\boldsymbol{P}}$ versus $\bar{\boldsymbol{F}}$ for the constrained case. (c) Domain-wise 11-component of $\bar{\boldsymbol{P}}$ versus $\bar{\boldsymbol{F}}$ for the unconstrained case. (d) Domain-wise 22-component of $\bar{\boldsymbol{P}}$ versus $\bar{\boldsymbol{F}}$ for the unconstrained case.

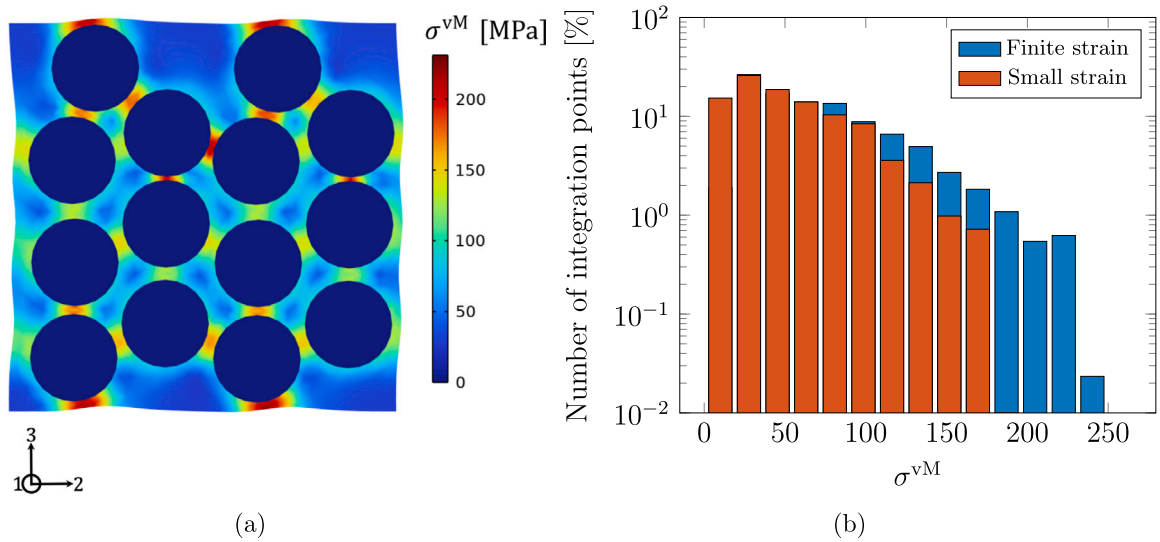

Fig. 6. Constrained RVE. (a) von Mises stress, σ^{vM}, in finite strain setting. The periodic fluctuation solution on the boundaries $\boldsymbol{u}^s$ is shown in a magnified state. (b) The distribution of the von Mises stress σ^{vM} in finite- and small strain setting for the constrained RVE. The stresses are computed at the integration point of each element in the matrix domain $\Omega_{\square}^{SBE}$ for the state $c = 1$.

and 22 direction. In this case, the SBE is extended (causing positive stresses) and the fibres are restricted to expand (causing negative stresses). Moreover, the RVE is stress free for all states of lithiation, c. Hence,

$$\bar{\boldsymbol{P}}_{UNCON}\{c, \bar{\boldsymbol{F}}_{UNCON}\} = V_{cf}\bar{\boldsymbol{P}}^{cf}\{c, \bar{\boldsymbol{F}}_{UNCON}\} + (1-V_{cf})\bar{\boldsymbol{P}}^{SBE}\{c, \bar{\boldsymbol{F}}_{UNCON}\} = \boldsymbol{0}, \tag{18}$$

where $V_{cf} = \frac{|\Omega_{\square}^{cf}|}{|\Omega_{\square}|}$ is the reference (unlithiated) volume fraction of carbon fibres. Thus, the sum of the homogenized stress for the two domains equals zero at all times.

3.2. Internal stress analysis

To analyse the internal stress state and assess the significance of the finite strain setting we apply the methods described in Section 2.2. Fig. 6a shows the distribution of the von Mises stress in $\Omega_{\square}^{SBE}$ at full state of lithiation for the externally constrained RVE using finite strains, computed as

$$\sigma^{vM} = \sqrt{\frac{3}{2}\boldsymbol{\sigma}_{dev} : \boldsymbol{\sigma}_{dev}} \text{ with } \boldsymbol{\sigma}_{dev} = \frac{1}{J}\left[\boldsymbol{P}\cdot\boldsymbol{F}^T - \frac{1}{3}[\boldsymbol{P} : \boldsymbol{F}]\boldsymbol{I}\right]. \tag{19}$$

Noticeably higher element stresses (magnitude) are predicted for the constrained case utilizing finite strains compared to small strain theory as shown in Fig. 6b. For the free, unconstrained RVE, lower stress magnitudes are found, as shown in Figs. 7a and 7b, which is expected considering the magnitude of the homogenized stresses in Figs. 5c and 5d. The difference in stress magnitudes using finite and small strain modelling indicates the significance of considering finite deformation theory. As strains inherently become large in the SBE between fibres, greater stress magnitudes are expected in these regions.

3.3. Effect of state of lithiation on the elastic moduli of the composite material

Here, the effect of state of lithiation on the longitudinal and transverse moduli of the negative electrode composite is evaluated. We solve the periodic RVE problem for both the constrained and unconstrained cases from Section 2.2, and evaluate the linearized tangent stiffness as described in Appendix C. To quantify the stiffness we identify an (assumed) transversely isotropic stiffness. The resulting moduli as function of c are shown in Figs. 8a and 8b. $\bar{E}_L$ is found to decrease slightly with an increase in c. In contrast, $\bar{E}_T$ is found to increase significantly with increasing c. Moreover, restricting expansion of the RVE gives an upper bound on the moduli, conversely the lower bound is obtained for the unconstrained RVE. At full state of lithiation, $\bar{E}_L$ is decreased by 3.2 % in the constrained case and by 6 % for the unconstrained case. In contrast, $\bar{E}_T$ is increased by 27 % for the constrained case and by 19 % for the unconstrained case at full state of lithiation. Comparing to the changes of the moduli in the carbon fibres (see Appendix B), the change in the composite stiffness is less pronounced for both the constrained and unconstrained case. Finally, a significant difference in the moduli computed in the small and finite strain settings can be observed. The effect of state of lithiation on $\bar{E}_L$ is overestimated when considering small strains, while the change in $\bar{E}_T$ is underestimated.

3.4. Electrode extension of the freely expanding RVE during electrochemical cycling

Carlstedt et al. monitored the free longitudinal expansion of a T800 carbon fibre electrode in a half-cell set-up, i.e., carbon fibre vs. lithium metal [9]. The available experiment represents an unconstrained composite, where measurements of the carbon fibre electrodes' longitudinal expansion during constant current, constant voltage (CCCV) cycling are plotted in Fig. 9. In Fig. 9(b,d), results for the free expansion of the T800 carbon fibre electrode in liquid electrolyte (LE) as well as in structural battery electrolyte (SBE) are presented. The lithiation process is initiated by a galvanostatic (current control) discharge followed by a potentiostatic (potential control) discharge, ensuring that the carbon fibres are completely filled with lithium. Comparing the expansions of the structural electrode in liquid electrolyte with the SBE electrode, the effective electrode expansion in SBE is significantly less than the electrode in liquid electrolyte. Moreover, during galvanostatic discharge, the pertinent effective expansion is linear with respect to time, whereas during potentiostatic discharge, the effective expansion response is nonlinear with respect to time. The apparent lithium concentration in the

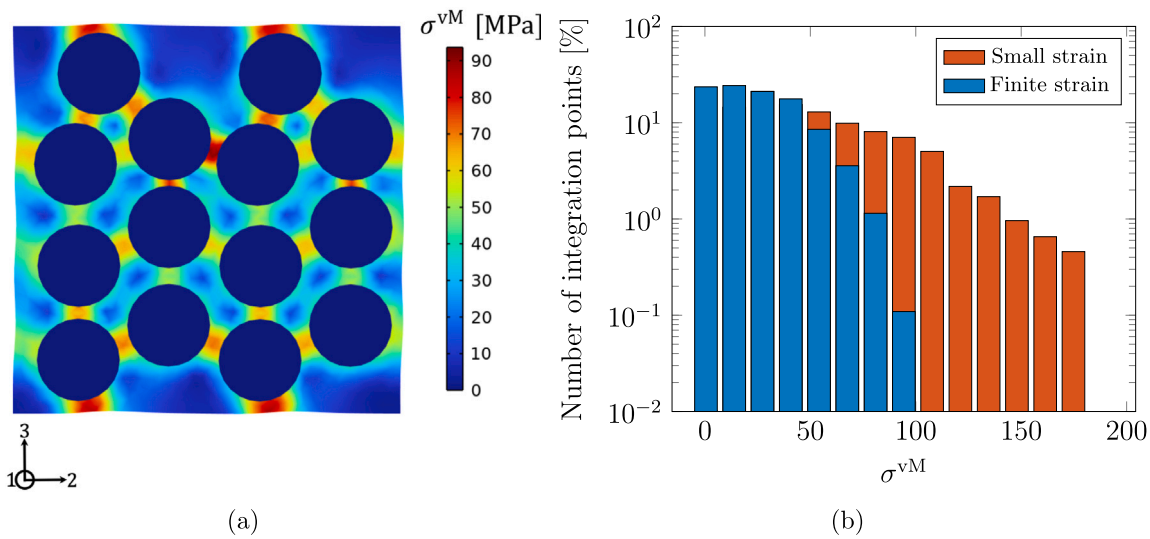

Fig. 7. Unconstrained RVE. (a) von Mises stress, σ^{vM}, in finite strain setting. The periodic fluctuation solution on the boundaries $\boldsymbol{u}^s$ is shown in a magnified state. (b) The distribution of the von Mises stress σ^{vM} in finite- and small strain setting in the unconstrained RVE. The stresses are computed at the integration point of each element in the matrix domain $\Omega_{\square}^{SBE}$ for the state $c = 1$.

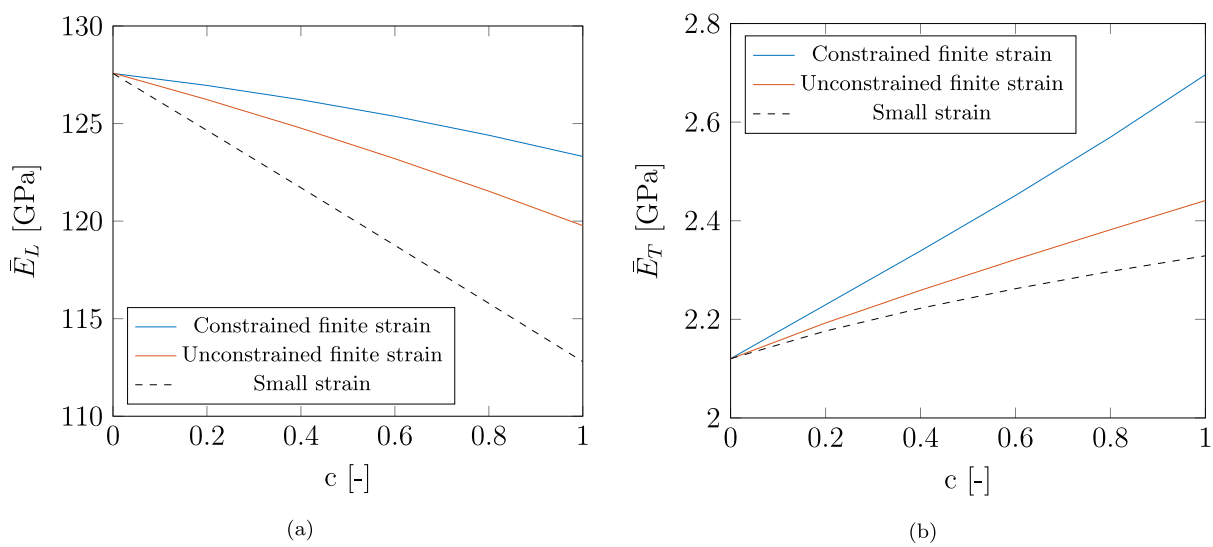

Fig. 8. (a) Homogenized longitudinal modulus, $\bar{E}_L$, with respect to state of lithiation, c, for constrained (blue) and unconstrained (red) configurations. (b) Homogenized transverse modulus, $\bar{E}_T$, with respect to state of lithiation, c. for constrained (blue) and unconstrained (red) configurations.

carbon fibre electrodes during each charge/discharge cycle is assessed by Faraday's law of electrolysis, considering the integrated current response from measurements presented in Figs. 9a and 9c according to

$$c_{Li}(t) = \frac{1}{nF}\int_0^t I\,\mathrm{d}t, \tag{20}$$

where F is Faradays constant and n represents the number of electrons transferred pertinent to the reaction. Fig. 10a shows how the amount of lithium in the carbon fibre electrode varies with time. The maximum amount of lithium that is inserted in the electrode varies between each charge/discharge cycle due to electrochemical losses and solid electrolyte interface (SEI) formation. Fig. 10b shows the expansion of the electrode presented in Fig. 9b versus the state of lithiation, c, for cycles 1, 3 and 5, where the maximum recorded electrode expansion is 0.85%.

Similar results are presented for the structural electrode in Fig. 11. In both cases, the current approaches zero at each charge/discharge cycle. This indicates that the carbon fibres are completely filled with lithium in each cycle, i.e. $c = 1$, for both the electrode in liquid electrolyte, and the structural electrode. Fig. 11a shows the lithium variation with time in the structural electrode, and Fig. 11b shows the axial expansion of the structural electrode for cycles 3 and 5. The proposed model is found to predict the free expansion of the structural electrode. Computed macroscopic stretch along the structural electrode, $\bar{U}_{11}$, is used to present the relative electrode expansion in Fig. 11b and exhibits a maximum expansion of $\bar{U}_{11} - 1 = 0.79$ %.

As expected, the relative expansion of the structural electrode is reduced by the SBE matrix. The SBE restricts the free expansion of the carbon fibres in the structural electrode by 0.06 % units at $c = 1$ for the given fibre arrangement and volume fraction. It is noteworthy that the adopted methodology allows for prediction of electrode expansion for any arrangement and volume fraction of the fibres.

4. Conclusions and outlook

In this paper, effects of the expansion and moduli for the carbon fibres, caused by a change in state of lithiation, on the mechanical

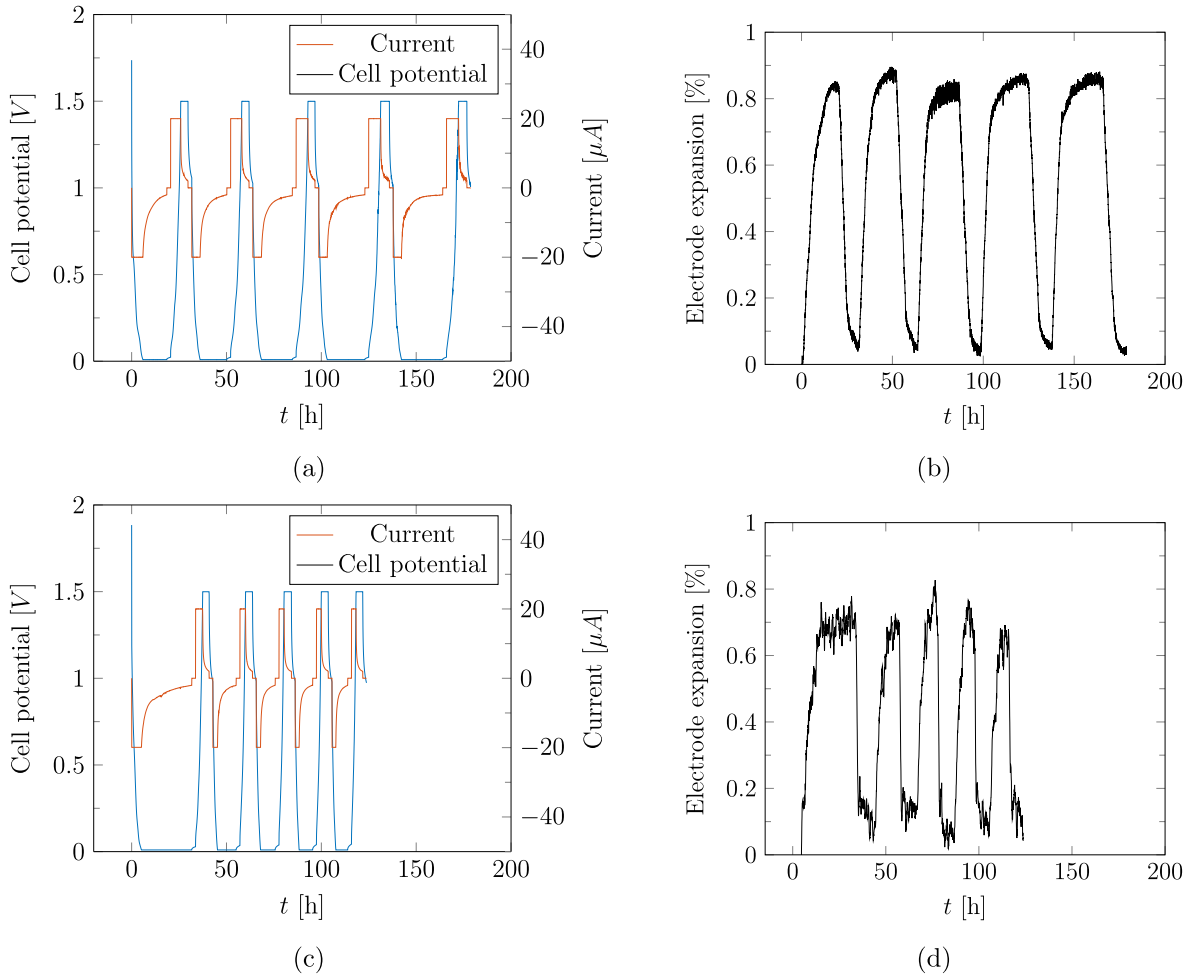

Fig. 9. (a) Experimental results from charge and discharge cycles of a carbon fibre electrode in liquid electrolyte. (b) Resulting relative fibre expansion caused by charge and discharge of carbon fibre in liquid electrolyte. (c) Experimental results of charge and discharge cycle of a structural carbon fibre electrode in SBE. (d) Resulting relative fibre expansion caused by charge and discharge of a structural carbon fibre electrode in SBE. The data presented in the figures above are obtained from [9].

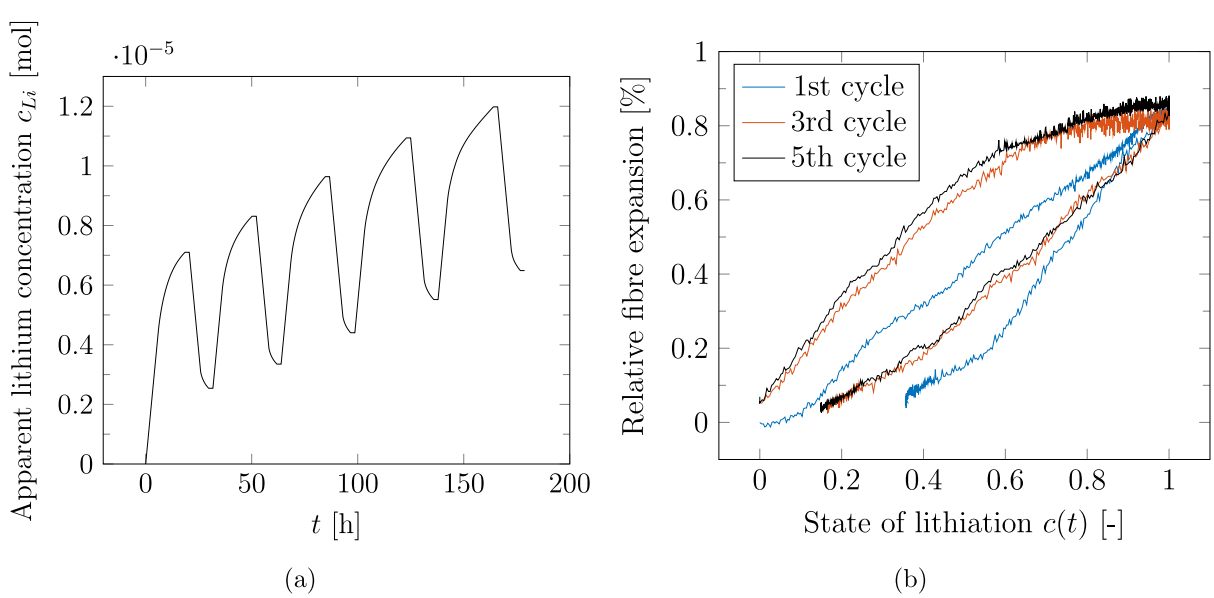

Fig. 10. (a) Total lithium concentration in the carbon fibre electrode in liquid electrolyte, extracted by integration of the current from Fig. 9a using Eq. (20). (b) Relative axial expansion with respect to state of lithiation, as defined in Eq. (2), for the 1st, 3rd and 5th charge/discharge cycle of the carbon fibre electrode in liquid electrolyte.

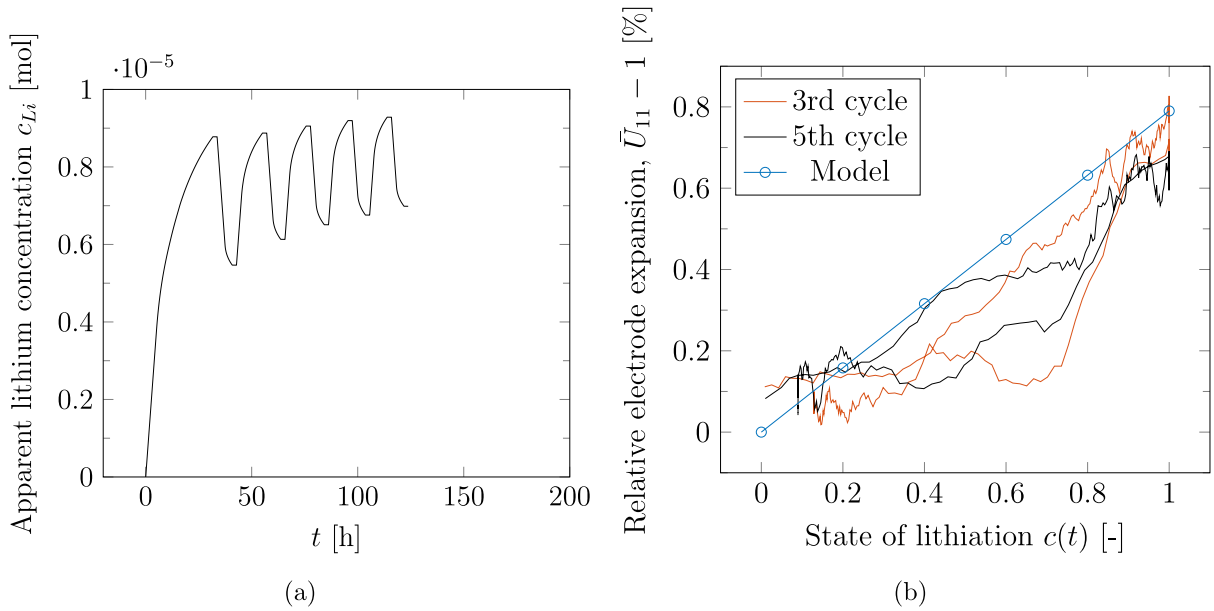

Fig. 11. (a) Total lithium concentration in the carbon fibre electrode in SBE, extracted by integration of the current from Fig. 9c using Eq. (20). (b) Relative longitudinal expansion with respect to state of lithiation, as defined in Eq. (2), for the 3rd and 5th charge/discharge cycle of the carbon fibre electrode embedded in SBE, as well as the relative expansion strain predicted by the model.

behaviour of the electrode are studied. Given the extensive swelling of the carbon fibre from lithium insertion, a computational model considering finite strains is proposed. More specifically, a multiplicative split is introduced to model the stress–strain response during arbitrarily sized expansion of carbon fibres due to lithiation, while fitting linearized anisotropic elasticity measurements for stress-free lithiated fibres. Numerical results show that the finite strain setting consideration is, indeed, needed to accurately predict the internal stress state and composite tangent stiffness at high states of lithiation of a structural negative electrode for the given fibre arrangement and volume fraction. Furthermore, the model is found to forecast the constraint on the fibres posed by the structural battery electrolyte, predicting the stress free expansion of the structural electrode during a constant current, constant voltage charge cycle. Thus, to accurately predict the internal stress state, as well as composite moduli and expansion of the carbon fibre-based structural electrode, finite strains must be considered.

Future studies should focus on quantifying local features within the composite through calibration and modelling of the SBE matrix under large deformations as well as performing statistical studies regarding fibre arrangement leading to proper representation of the microstructure.

CRediT authorship contribution statement

Carl Larsson: Methodology, Conceptualization, Writing – original draft, Writing – review & editing. **Fredrik Larsson:** Methodology, Supervision, Writing – original draft, Writing – review & editing. **Johanna Xu:** Methodology, Supervision, Writing – review & editing. **Kenneth Runesson:** Methodology, Writing – review & editing. **Leif E. Asp:** Methodology, Supervision, Funding, Writing – original draft, Writing – review & editing.

Declaration of competing interest

The authors declare that they have no known competing financial interests or personal relationships that could have appeared to influence the work reported in this paper.

Data availability

Data will be made available on request

Acknowledgements

The project is funded by the USAF via the EOARD Award No. FA8655-21-1-7038, ONR, USA, Award No. N62909-22-1-2037, the Swedish National Space Agency, project no. 2020-00256, Swedish Research Council, grant number 2020-05057, and 2D TECH VINNOVA competence Center, grant number 2019-00068.

Appendix A. The stress controlled problem

To enable the representation of an unconstrained RVE, we wish to control the macroscopic stress $\bar{\boldsymbol{P}}$ as defined in Eq. (5). However, the problem of seeking the macroscopic deformation $\bar{\boldsymbol{F}}$ for a given $\bar{\boldsymbol{P}}$ is ill-posed due to rigid-body in-variance. Consider the polar decomposition of $\bar{\boldsymbol{F}}$ into the proper orthonormal tensor $\bar{\boldsymbol{R}}$, representing rigid body rotation, and the symmetric right stretch tensor $\bar{\boldsymbol{U}}$ such that $\bar{\boldsymbol{F}} = \bar{\boldsymbol{R}} \cdot \bar{\boldsymbol{U}}$. Firstly, we establish that $\bar{\boldsymbol{P}}$ is objective w.r.t. macroscopic rotations, i.e.,

$$\begin{aligned}\bar{\boldsymbol{P}}\{\bar{\boldsymbol{R}}^* \cdot \bar{\boldsymbol{F}}\} &= \frac{1}{\Omega_{X,\square}} \int_{\Omega_{X,\square}} \boldsymbol{P}(\bar{\boldsymbol{R}}^* \cdot \bar{\boldsymbol{F}} + [\boldsymbol{u}^s\{\bar{\boldsymbol{R}}^* \cdot \bar{\boldsymbol{F}}\} \otimes \boldsymbol{\nabla}_X])\mathrm{d}\Omega_X \\ &= \frac{1}{\Omega_{X,\square}} \int_{\Omega_{X,\square}} \boldsymbol{P}(\bar{\boldsymbol{R}}^* \cdot \bar{\boldsymbol{F}} + \bar{\boldsymbol{R}}^* \cdot [\boldsymbol{u}^s\{\bar{\boldsymbol{F}}\} \otimes \boldsymbol{\nabla}_X])\mathrm{d}\Omega_X \\ &= \bar{\boldsymbol{R}}^* \cdot \frac{1}{\Omega_{X,\square}} \int_{\Omega_{X,\square}} \boldsymbol{P}(\bar{\boldsymbol{F}} + [\boldsymbol{u}^s\{\bar{\boldsymbol{F}}\} \otimes \boldsymbol{\nabla}_X])\mathrm{d}\Omega_X = \bar{\boldsymbol{R}}^* \cdot \bar{\boldsymbol{P}}\{\bar{\boldsymbol{F}}\},\end{aligned} \tag{A.1}$$

for any rotation $\bar{\boldsymbol{R}}^*$. Relation (A.1) holds for any objective fine scale constitutive model satisfying $\boldsymbol{P}(\boldsymbol{R}^* \cdot \boldsymbol{F}) = \boldsymbol{R}^* \cdot \boldsymbol{P}(\boldsymbol{F})$, and for the chosen boundary conditions that ensure $\boldsymbol{u}^s\{\bar{\boldsymbol{R}}^* \cdot \bar{\boldsymbol{F}}\} = \bar{\boldsymbol{R}}^* \cdot \boldsymbol{u}^s\{\bar{\boldsymbol{F}}\}$. Hence, we conclude that

$$\bar{\boldsymbol{P}}\{\bar{\boldsymbol{F}}\} = \bar{\boldsymbol{P}}\{\bar{\boldsymbol{R}} \cdot \bar{\boldsymbol{U}}\} = \bar{\boldsymbol{R}} \cdot \bar{\boldsymbol{P}}\{\bar{\boldsymbol{U}}\}, \tag{A.2}$$

where the last identity follows from (A.1). Thus, it suffices to determine $\bar{\boldsymbol{P}}^U\{\bar{\boldsymbol{U}}\} := \bar{\boldsymbol{P}}\{\bar{\boldsymbol{U}}\}$ where $\bar{\boldsymbol{P}}^U : \mathbb{R}^{3\times3}_{\mathrm{sym}} \to \mathbb{R}^{3\times3}$. Next, by identification, the symmetric Biot stress $\bar{\boldsymbol{T}} := [\bar{\boldsymbol{R}}^T \cdot \bar{\boldsymbol{P}}]^{\mathrm{sym}} = [\bar{\boldsymbol{P}}^U]^{\mathrm{sym}}$. Hence, stress control for the RVE-problem can be stated as follows:

Table B.1
Mechanical properties for the carbon fibres and SBE.

Carbon fibres	Source
$E_L = 294(1-0.12c)$ GPa	[10]
$E_T = 21.8(1+1.07c)$ GPa	[10]
$\nu_{TT} = 0.2$	Assumed
$\nu_{LT} = 0.22$	Assumed
$\alpha_T = 0.066$	[10]
$\alpha_L = 0.0085$	[9]
$G_{LT} = 12.5$ GPa	Assumed
SBE	
$E = 0.700$ GPa	[22]
$\nu = 0.37$	Assumed

For known $\bar{\boldsymbol{T}}$, find $\left(\boldsymbol{u}^{s,*}\{\bar{\boldsymbol{T}}\}, \bar{\boldsymbol{U}}\{\bar{\boldsymbol{T}}\}\right) = \left(\boldsymbol{u}^{s,*}, \bar{\boldsymbol{U}}\right) \in \mathbb{U}_\square \times \mathbb{R}^{3\times3}_{\text{sym}}$ such that

$$\frac{1}{|\Omega_{X,\square}|}\int_{\Omega_{X,\square}} \boldsymbol{P}(\bar{\boldsymbol{U}} + \boldsymbol{u}^{s,*} \otimes \boldsymbol{\nabla}_X) : [\delta\boldsymbol{u}^s \otimes \boldsymbol{\nabla}_X]\mathrm{d}\Omega_X = 0 \quad \forall \delta\boldsymbol{u}^s \in \mathbb{U}_\square, \tag{A.3a}$$

$$\frac{1}{|\Omega_{X,\square}|}\int_{\Omega_{X,\square}} \boldsymbol{P}(\bar{\boldsymbol{U}} + \boldsymbol{u}^{s,*} \otimes \boldsymbol{\nabla}_X)\mathrm{d}\Omega_X : \delta\bar{\boldsymbol{U}} = \bar{\boldsymbol{T}} : \delta\bar{\boldsymbol{U}} \quad \forall \delta\bar{\boldsymbol{U}} \in \mathbb{R}^{3\times3}_{\text{sym}}, \tag{A.3b}$$

where $\boldsymbol{u}^{s,*} = \bar{\boldsymbol{R}}^{-1} \cdot \boldsymbol{u}^s$. For a given rotation $\bar{\boldsymbol{R}}$, the result may be interpreted as $\bar{\boldsymbol{F}} = \bar{\boldsymbol{R}} \cdot \bar{\boldsymbol{U}}\{\bar{\boldsymbol{T}}\}$ and

$$\bar{\boldsymbol{P}} = \bar{\boldsymbol{R}} \cdot \bar{\boldsymbol{P}}^U = \bar{\boldsymbol{R}} \cdot \frac{1}{|\Omega_{X,\square}|}\int_{\Omega_{X,\square}} \boldsymbol{P}(\bar{\boldsymbol{U}}\{\bar{\boldsymbol{T}}\} + [\boldsymbol{u}^{s,*}\{\bar{\boldsymbol{T}}\} \otimes \boldsymbol{\nabla}_X])\mathrm{d}\Omega_X. \tag{A.4}$$

Appendix B. Constitutive modelling of the carbon fibre domain

[H] The transversely isotropic linear elastic stiffness tensor for a lithiated carbon fibre in the (stress-free) configuration $\tilde{\boldsymbol{B}}$ is expressed as[2]

$$\begin{aligned}\tilde{\mathbf{E}}(c) &= L_T(c)\boldsymbol{I} \otimes \boldsymbol{I} + 2G_{TT}(c)\mathbf{I}^{\text{sym}} + [L_L(c) - L_T(c)][\boldsymbol{I} \otimes \boldsymbol{m}_1 + \boldsymbol{m}_1 \otimes \boldsymbol{I}] + \\ &[H_L(c) - 4G_{LT} + 2G_{TT}(c) - 2L_L(c) + L_T(c)]\boldsymbol{m}_1 \otimes \boldsymbol{m}_1 + 4[G_{LT} - G_{TT}(c)]\mathbf{A}.\end{aligned} \tag{B.1}$$

with $\mathbf{A} = \frac{1}{4}(\boldsymbol{m}_1 \bar{\otimes} \boldsymbol{I} + \boldsymbol{m}_1 \underline{\otimes} \boldsymbol{I} + \boldsymbol{I} \bar{\otimes} \boldsymbol{m}_1 + \boldsymbol{I} \underline{\otimes} \boldsymbol{m}_1)$, $H_L = \frac{E_L(1-\nu_{TT}^2)}{(1+\nu_{TT})(1-\nu_{TT}-2\nu_{LT}^2 E_T/E_L)}$, $L_T = \frac{E_T(\nu_{TT}+\nu_{LT}^2 E_T/E_L)}{(1+\nu_{TT})(1-\nu_{TT}-2\nu_{LT}^2 E_T/E_L)}$ and $L_L = \frac{E_T \nu_{LT}}{(1-\nu_{TT}-2\nu_{LT}^2 E_T/E_L)}$. The experimentally obtained parameters are stated in Table B.1. Using the Saint-Venant model in Eqs. (13), we can formulate the second Piola–Kirchhoff stress in the reference configuration on the form

$$\boldsymbol{S} = \mathbf{L}_2(c) : [\frac{1}{2}(\boldsymbol{F}^T \cdot \boldsymbol{F} - [\boldsymbol{F}^{\text{ch}}(c)]^T \cdot \boldsymbol{F}^{\text{ch}}(c))], \tag{B.2}$$

where the tangent operator of the second Piola–Kirchhoff stress is obtained as

$$\mathbf{L}_2(c) = J^{\text{ch}}(c)\left([\boldsymbol{F}^{\text{ch}}(c)]^{-1} \bar{\otimes} [\boldsymbol{F}^{\text{ch}}(c)]^{-1}\right) : \tilde{\mathbf{E}}(c) : \left([\boldsymbol{F}^{\text{ch}}(c)]^{-T} \bar{\otimes} [\boldsymbol{F}^{\text{ch}}(c)]^{-T}\right). \tag{B.3}$$

Finally, we express the tangent operator of the first Piola–Kirchhoff stress as

$$\mathbf{L}(\boldsymbol{F}, c) = [\boldsymbol{F} \bar{\otimes} \boldsymbol{I}] : \mathbf{L}_2(c) : [\boldsymbol{F}^T \otimes \boldsymbol{I}] + \boldsymbol{I} \bar{\otimes} \boldsymbol{S}(\boldsymbol{F}, c). \tag{B.4}$$

[2] Here, we introduce the open product operators $(\boldsymbol{B} \otimes \boldsymbol{C})_{ijkl} = B_{ij}C_{kl}$, $(\boldsymbol{B} \bar{\otimes} \boldsymbol{C})_{ijkl} = B_{ik}C_{jl}$ and $(\boldsymbol{B} \underline{\otimes} \boldsymbol{C})_{ijkl} = B_{il}C_{jk}$, for second order tensors $\boldsymbol{B}$ and $\boldsymbol{C}$, and the base dyad $\boldsymbol{m}_1 = \boldsymbol{e}_1 \otimes \boldsymbol{e}_1$ for basis vector $\boldsymbol{e}_1$ in the L-direction.

Appendix C. Homogenized tangent stiffness

To establish how the mechanical properties of the composite vary with he state of lithiation, c, we consider $\bar{\boldsymbol{P}}$ linearized w.r.t. $\bar{\boldsymbol{F}}$. Thereby, we express the tangent stiffness as

$$\bar{\mathbf{L}}\{c, \bar{\boldsymbol{F}}\} = \frac{\mathrm{d}\bar{\boldsymbol{P}}}{\mathrm{d}\bar{\boldsymbol{F}}}. \tag{C.1}$$

The linearized form of Eqs. (4) and (5) become that of finding $\mathrm{d}\boldsymbol{u}^s \in \mathbb{U}_\square$ such that

$$\begin{aligned}&\frac{1}{|\Omega_{X,\square}|}\int_{\Omega_{X,\square}} [\delta\boldsymbol{u}^s \otimes \boldsymbol{\nabla}_X] : \mathbf{L}(c, \bar{\boldsymbol{F}} + \boldsymbol{u}^s \otimes \boldsymbol{\nabla}_X) : [\mathrm{d}\boldsymbol{u}^s \otimes \boldsymbol{\nabla}_X]\mathrm{d}\Omega_X \\ &+ \frac{1}{|\Omega_{X,\square}|}\int_{\Omega_{X,\square}} [\delta\boldsymbol{u}^s \otimes \boldsymbol{\nabla}_X] : \mathbf{L}(c, \bar{\boldsymbol{F}} + \boldsymbol{u}^s \otimes \boldsymbol{\nabla}_X)\mathrm{d}\Omega_X : \mathrm{d}\bar{\boldsymbol{F}} = 0 \quad \forall \delta\boldsymbol{u}^s \in \mathbb{U}_\square,\end{aligned} \tag{C.2}$$

and expressing

$$\begin{aligned}\mathrm{d}\bar{\boldsymbol{P}} &= \frac{1}{|\Omega_{X,\square}|}\int_{\Omega_{X,\square}} \mathbf{L}(c, \bar{\boldsymbol{F}} + \boldsymbol{u}^s \otimes \boldsymbol{\nabla}_X)\mathrm{d}\Omega_X : \mathrm{d}\bar{\boldsymbol{F}} \\ &+ \frac{1}{|\Omega_{X,\square}|}\int_{\Omega_{X,\square}} \mathbf{L}(c, \bar{\boldsymbol{F}} + \boldsymbol{u}^s \otimes \boldsymbol{\nabla}_X) : [\mathrm{d}\boldsymbol{u}^s \otimes \boldsymbol{\nabla}_X]\mathrm{d}\Omega_X.\end{aligned} \tag{C.3}$$

Since $\bar{\boldsymbol{F}}$ and $\boldsymbol{u}^s\{\bar{\boldsymbol{F}}\}$ are fixed, we utilize the linearity of Eqs. (C.2) and (C.3) to express $\mathrm{d}\bar{\boldsymbol{F}} = \sum_{i,j} \boldsymbol{e}_i \otimes \boldsymbol{e}_j \mathrm{d}\bar{F}_{ij} \rightarrow \mathrm{d}\boldsymbol{u}^s = \sum_{i,j} \hat{\boldsymbol{u}}^{s(ij)}\{\bar{\boldsymbol{F}}, \mathrm{d}\bar{\boldsymbol{F}}\}\mathrm{d}\bar{F}_{ij}$, where the sensitivities $\hat{\boldsymbol{u}}^{s(ij)} \in \mathbb{U}_\square$ are solved from

$$\begin{aligned}&\frac{1}{|\Omega_{X,\square}|}\int_{\Omega_{X,\square}} [\delta\boldsymbol{u}^s \otimes \boldsymbol{\nabla}_X] : \mathbf{L} : [\hat{\boldsymbol{u}}^{s(ij)} \otimes \boldsymbol{\nabla}_X]\mathrm{d}\Omega_X = \\ &-\frac{1}{|\Omega_{X,\square}|}\int_{\Omega_{X,\square}} [\delta\boldsymbol{u}^s \otimes \boldsymbol{\nabla}_X] : \mathbf{L} : [\boldsymbol{e}_i \otimes \boldsymbol{e}_j]\mathrm{d}\Omega_X \quad \forall \delta\boldsymbol{u}^s \in \mathbb{U}_\square\end{aligned} \tag{C.4}$$

for $i, j \in \{1, 2, 3\}^2$. Thereby,

$$\begin{aligned}\mathrm{d}\bar{\boldsymbol{P}} &= \sum_{i,j} \frac{1}{|\Omega_{X,\square}|}\int_{\Omega_{X,\square}} \mathbf{L} : [(\boldsymbol{e}_i \otimes \boldsymbol{e}_j) + (\hat{\boldsymbol{u}}^{s(ij)} \otimes \boldsymbol{\nabla}_X)]\mathrm{d}\Omega_X \mathrm{d}\bar{F}_{ij} \\ &= \left(\sum_{i,j} \frac{1}{|\Omega_{X,\square}|}\int_{\Omega_{X,\square}} \mathbf{L} : [(\boldsymbol{e}_i \otimes \boldsymbol{e}_j) + (\hat{\boldsymbol{u}}^{s(ij)} \otimes \boldsymbol{\nabla}_X)]\mathrm{d}\Omega_X \otimes [\boldsymbol{e}_i \otimes \boldsymbol{e}_j]\right) : \mathrm{d}\bar{\boldsymbol{F}}.\end{aligned} \tag{C.5}$$

Eq. (C.5) represents an exact differential. Thus, we conclude that $\mathrm{d}\bar{\boldsymbol{P}} = \bar{\mathbf{L}}(c, \bar{\boldsymbol{F}}) : \mathrm{d}\bar{\boldsymbol{F}}$, where the tangent stiffness is

$$\bar{\mathbf{L}} = \sum_{i,j} \hat{\boldsymbol{P}}^{(ij)} \otimes \boldsymbol{e}_i \otimes \boldsymbol{e}_j, \tag{C.6a}$$

and

$$\hat{\boldsymbol{P}}^{(ij)} = \frac{1}{\Omega_{X,\square}}\int_{\Omega_{X,\square}} \mathbf{L}(c, \bar{\boldsymbol{F}} + \boldsymbol{u}^s \otimes \boldsymbol{\nabla}_X) : [(\boldsymbol{e}_i \otimes \boldsymbol{e}_j) + (\hat{\boldsymbol{u}}^{s(ij)} \otimes \boldsymbol{\nabla}_X)]\mathrm{d}\Omega_X. \tag{C.6b}$$

The tangent stiffness as expressed in Eq. (C.6a) is described in the reference configuration Ω_X. To express the stiffness tensor in the deformed configuration $\bar{\Omega}_X \rightarrow \bar{\Omega}$, we express the apparent small strain Hooke tensor corresponding to an updated Lagrangian formulation as

$$\bar{\mathbf{E}} = \frac{1}{J}[\boldsymbol{I} \bar{\otimes} \bar{\boldsymbol{F}}] : \bar{\mathbf{L}} : [\boldsymbol{I} \bar{\otimes} \bar{\boldsymbol{F}}^T]. \tag{C.7}$$

In order to analyse the results, we identify the apparent transversely isotropic parameters $\bar{E}_L$, $\bar{E}_T$ and $\bar{G}_{LT}$, and Poisson's ratio $\bar{\nu}_{LT}$. Extracted from the optimization problem formulated as

$$\min_{\bar{E}_L, \bar{E}_T, \bar{G}_{LT}, \bar{\nu}_{LT}} \sqrt{\sum_{ijkl} (\mathbf{E}(\bar{E}_L, \bar{E}_T, \bar{G}_{LT}, \bar{\nu}_{LT}) - \bar{\mathbf{E}})^2_{ijkl}}, \tag{C.8}$$

where $\mathbf{E}(\bar{E}_L, \bar{E}_T, \bar{G}_{LT}, \bar{\nu}_{LT})$ is the (explicit) parametrized fourth order elastic stiffness tensor pertinent to transverse isotropy.

References

[1] L.E. Asp, M. Johansson, G. Lindbergh, J. Xu, D. Zenkert, Structural battery composites: A review, Funct. Compos. Struct. 1 (2019) 042001.

[2] L.E. Asp, et al., A structural battery and its multifunctional performance, Adv. Energy Sustain. Res. 2 (2021) 2000093.

[3] K. Moyer, et al., Carbon fiber reinforced structural lithium-ion battery composite: Multifunctional power integration for CubeSats, Energy Storage Mater. 24 (2020) 676–681.

[4] G.J. Lim, K.K. Chan, N.A. Sutrisnoh, M. Srinivasan, Design of structural batteries: carbon fibers and alternative form factors, Mater. Today Sustain. 20 (2022) 100252.

[5] J. Hagberg, et al., Lithium iron phosphate coated carbon fiber electrodes for structural lithium ion batteries, Compos. Sci. Technol. 162 (2018) 235–243.

[6] J.S. Sanchez, J. Xu, Z. Xia, J. Sun, L.E. Asp, V. Palermo, Electrophoretic coating of LiFePO4/Graphene oxide on carbon fibers as cathode electrodes for structural lithium ion batteries, Compos. Sci. Technol. 208 (2021) 108768.

[7] L.M. Schneider, N. Ihrner, D. Zenkert, M. Johansson, Bicontinuous electrolytes via thermally initiated polymerization for structural lithium ion batteries, ACS Appl. Energy Mater. 2 (2019) 4362–4369.

[8] M.H. Kjell, E. Jacques, D. Zenkert, M. Behm, G. Lindbergh, PAN-based carbon fiber negative electrodes for structural lithium-ion batteries, J. Electrochem. Soc. 158 (2011) A1455.

[9] D. Carlstedt, et al., Experimental and computational characterization of carbon fibre based structural battery electrode laminae, Compos. Sci. Technol. 220 (2022) 109283.

[10] S. Duan, et al., Effect of lithiation on the elastic moduli of carbon fibres, Carbon 185 (2021) 234–241.

[11] D. Carlstedt, K. Runesson, F. Larsson, J. Xu, L.E. Asp, Electro-chemo-mechanically coupled computational modelling of structural batteries, Multifunct. Mater. 3 (2020) 045002.

[12] D. Carlstedt, K. Runesson, F. Larsson, L.E. Asp, On the coupled thermo–electro–chemo–mechanical performance of structural batteries with emphasis on thermal effects, Eur. J. Mech. A Solids 94 (2022) 104586.

[13] D. Grazioli, O. Verners, V. Zadin, D. Brandell, A. Simone, Electrochemical-mechanical modeling of solid polymer electrolytes: Impact of mechanical stresses on Li-ion battery performance, Electrochim. Acta 296 (2019) 1122–1141.

[14] G. Bucci, Y.M. Chiang, W.C. Carter, Formulation of the coupled electrochemical-mechanical boundary-value problem, with applications to transport of multiple charged species, Acta Mater. 104 (2016) 33–51.

[15] M. Ganser, F.E. Hildebrand, M. Kamlah, R.M. McMeeking, A finite strain electro-chemo-mechanical theory for ion transport with application to binary solid electrolytes, J. Mech. Phys. Solids 125 (2019) 681–713.

[16] M.S. Siraj, S. Tasneem, D. Carlstedt, S. Duan, M. Johansen, C. Larsson, J. Xu, F. Liu, F. Edgren, L.E. Asp, Advancing structural battery composites: Robust manufacturing for enhanced and consistent multifunctional performance, Adv. Energy Sustain. Res. (2023) 2300109.

[17] N.P. van Dijk, Formulation and implementation of stress-driven and/or strain-driven computational homogenization for finite strain, Internat. J. Numer. Methods Engrg. 107 (2016) 1009–1028.

[18] E.A. de Souza Neto, R.A. Feijóo, On the equivalence between spatial and material volume averaging of stress in large strain multi-scale solid constitutive models, Mech. Mater. 40 (2008) 803–811.

[19] I.A.R. Lopes, F.M.A. Pires, Formulation and numerical implementation of a variationally consistent multi-scale model based on second-order computational homogenisation at finite strains for quasi-static problems, Comput. Methods Appl. Mech. Engrg. 392 (2022).

[20] S. Saeb, P. Steinmann, A. Javili, Aspects of computational homogenization at finite deformations: A unifying review from Reuss' to Voigt's bound, Appl. Mech. Rev. 68 (2016) 050801.

[21] D. Carlstedt, K. Runesson, F. Larsson, V. Tu, R. Jänicke, L.E. Asp, Computational modelling of structural batteries accounting for stress-assisted convection in the electrolyte, Int. J. Solids Struct. 238 (2022) 111343.

[22] S. Duan, M. Cattaruzza, V. Tu, R.M. Auenhammer, R. Jänicke, M.K.G. Johansson, F. Liu, L.E. Asp, Three-dimensional reconstruction and computational analysis of a structural battery composite electrolyte, Commun. Mater. 4 (2023).